Progress in Oceanography 187 (2020) 102396

Contents lists available at ScienceDirect

Progress in Oceanography

journal homepage: www.elsevier.com/locate/pocean

Circulation in the vicinity of Mackenzie Canyon from a year-long mooring array

Peigen Lin[a,*], Robert S. Pickart[a], David Fissel[b], Ed Ross[b], Jeremy Kasper[c], Frank Bahr[a], Daniel J. Torres[a], Jeff O'Brien[a], Keath Borg[b], Humfrey Melling[d], Francis K. Wiese[e]

[a] Woods Hole Oceanographic Institution, Woods Hole, MA, USA
[b] ASL Environmental Sciences Inc., Victoria, BC, Canada
[c] Institute of Northern Engineering, University of Alaska Fairbanks, Fairbanks, AK, USA
[d] Fisheries and Oceans Canada, Institute of Ocean Sciences, Sidney, BC, Canada
[e] Stantec Consulting Services Inc., Anchorage, AK, USA

ARTICLE INFO

Keywords:
Canadian Beaufort Sea
Mackenzie Canyon
Boundary currents
Canyon circulation
Ice-ocean interaction

ABSTRACT

Data from a five-mooring array extending from the inner shelf to the continental slope in the vicinity of Mackenzie Canyon, Beaufort Sea are analyzed to elucidate the components of the boundary current system and their variability. The array, part of the Marine Arctic Ecosystem Study (MARES), was deployed from October 2016 to September 2017. Four distinct currents were identified: an eastward-directed flow adjacent to the coast; a westward-flowing, surface-intensified current centered on the outer-shelf; a bottom-intensified shelfbreak jet flowing to the east; and a recirculation at the base of the continental slope within the canyon. The shelf current transports −0.12±0.03 Sv in the mean and is primarily wind-driven. The response is modulated by the presence of ice, with little-to-no signal during periods of nearly-immobile ice cover and maximum response when there is partial ice cover. The shelfbreak jet transports 0.03±0.02 Sv in the mean, compared to 0.08±0.02 Sv measured upstream in the Alaskan Beaufort Sea over the same time period. The loss of transport is consistent with a previous energetics analysis and the lack of Pacific-origin summer water downstream. The recirculation in the canyon appears to be the result of local dynamics whereby a portion of the westward-flowing southern limb of the Beaufort Gyre is diverted up the canyon across isobaths. This interpretation is supported by the fact that the low-frequency variability of the recirculation is correlated with the wind-stress curl in the Canada Basin, which drives the Beaufort gyre.

1. Introduction

Pacific-origin water flows northward through Bering Strait, driven primarily by the meridional sea surface height gradient (Aagaard et al., 2006; Woodgate, 2018), supplying heat, freshwater, and nutrients to the Arctic Ocean. The inflow has three main pathways across the Chukchi Shelf: one to the west which passes through Herald Canyon, another which is steered through Central Channel between Herald and Hanna Shoals, and a third that flows along the Alaskan coast which in summertime is referred to as the Alaskan Coastal Current (Fig. 1a; Woodgate et al., 2005; Brugler et al., 2014; Lin et al., 2019a). Much of the Pacific water drains off the Chukchi Shelf through Barrow Canyon (Itoh et al., 2013; Gong and Pickart, 2015; Pickart et al., 2016), contributing to the Beaufort shelfbreak jet to the east (Pickart, 2004; Nikolopoulos et al., 2009) and the Chukchi Slope Current to the west (Fig. 1a; Corlett and Pickart, 2017; Spall et al., 2018; Li et al., 2019).

East of Barrow Canyon the Beaufort shelfbreak jet has a strong seasonal cycle in its kinematic structure, volume transport, and the water it advects (Pickart 2004; Nikolopoulos et al., 2009; Brugler et al., 2014). In summertime the jet is surface-intensified and carries Pacific summer water masses, while during the remainder of the year it is bottom-intensified and carries cold Pacific winter waters. The transport peaks in summer, accounting for roughly 85% of the annually averaged value. Over the ten-year period from 2002 to 2012 the transport diminished considerably from 0.13±0.08 Sv (average from 2002 to 3, Nikolopoulos et al., 2009) to 0.03±0.01 Sv (average from 2008 to 12, Lin et al., 2016). This decrease in volume flux has been attributed to strengthened easterly summertime winds which oppose the shelfbreak jet. Dynamically, the alongcoast wind alters the strength of the current by changing the cross-shelf sea surface height gradient. Lin et al. (2016)

* Corresponding author.
E-mail address: plinwhoi@gmail.com (P. Lin).

https://doi.org/10.1016/j.pocean.2020.102396
Received 23 December 2019; Received in revised form 26 June 2020; Accepted 26 June 2020
Available online 04 July 2020
0079-6611/ © 2020 The Author(s). Published by Elsevier Ltd. This is an open access article under the CC BY-NC-ND license (http://creativecommons.org/licenses/BY-NC-ND/4.0/).

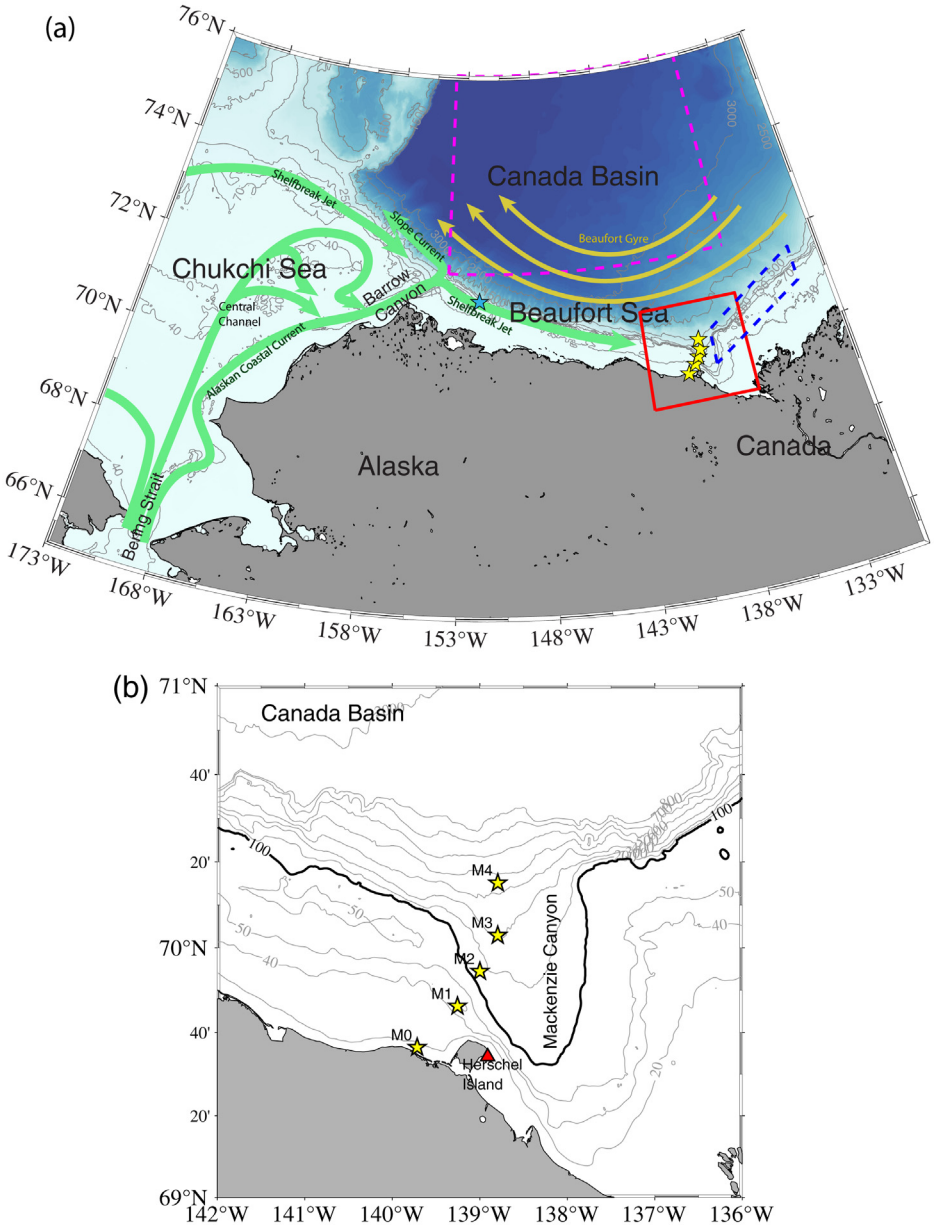

Fig. 1. (a) Schematic circulation of the Chukchi and Beaufort Seas and various place names. The green arrows represent the circulation of Pacific-origin water, and the yellow arrows denote the southern part of the Beaufort Gyre. The five moorings comprising the MARES array in Canadian Beaufort Sea are indicated by the yellow stars. The 152°W mooring in Alaskan Beaufort Sea (e.g. Lin et al., 2016) is marked by the blue star. The red box denotes the study region shown in (b). The dashed blue and magenta boxes are the regions over which the surface geostrophic velocities and wind stress curl are averaged, respectively (Section 5, Figs. 13 and 14). (b) Enlarged view of the study region. Bathymetry contours, from IBCAO version 3, are in meters; the 100 m isobath, delimiting the rim of Mackenzie Canyon, is highlighted by the thick contour. The red triangle marks the location of the Herschel Island meteorological station.

decomposed the total transport of the current into a background component, when the wind is weak, and a wind-forced component which correlates well with the along-coast wind stress. They found that the shelfbreak jet was wind-forced 72% of time during the study period from 2008 to 2012.

Using data from a two-year mooring array in the Alaskan Beaufort Sea, von Appen and Pickart (2012) estimated the spin-down distance of the Beaufort shelfbreak jet due to energy extraction from the current by hydrodynamic instability. They deduced that the summertime configuration of the flow (surface-intensified) should not persist beyond the eastern end of the Alaskan Beaufort Sea, but that the wintertime configuration (bottom-intensified) would extend beyond the first entrance to the Canadian Arctic Archipelago. Mooring observations indicate that the jet does exist in the Canadian Beaufort Sea. Kulikov et al. (1998) presented data from the Mackenzie shelfbreak where the flow was stronger in the lower layer (130 m) than the upper layer (35 m), consistent with a bottom-trapped current. A shelfbreak jet was also measured more recently, and over a longer period of time, using moorings deployed in the same area (Forest et al., 2015). It is still unclear how far the jet progresses, although Pacific water is found in Fram Strait and northeast of Greenland (e.g. Jones et al., 2003; Rudels et al., 2004). However, the water could have reached these locations from an interior route via the transpolar drift (Steele et al., 2004).

The dominant sub-inertial variability along the shelfbreak, both in the Alaskan and Canadian Beaufort Seas, is due to wind-forced upwelling and downwelling which leads to shelf-basin exchange of heat, salt, nutrients, and carbon (Macdonald et al., 1987; Pickart et al., 2011; 2013). Upwelling is driven by easterly winds arising from the interplay between the Aleutian Low and Beaufort High (e.g. Pickart et al., 2009; Kirillov et al., 2016), which tend to temporarily reverse the shelfbreak jet. In the Alaskan Beaufort Sea these events occur throughout the year and during all ice conditions (Schulze and Pickart, 2012), although there is a clear seasonality in terms whether Pacific-origin or Atlantic-origin water is upwelled from the basin (Lin et al., 2019b). Downwelling transports water from the base of the shelf into the interior, a process that helps ventilate the upper halocline in the Canada Basin (Foukal et al. 2019). During these events the shelfbreak jet is accelerated to the east (Dmitrenko et al., 2016; Foukal et al., 2019). Downwelling is associated with westerly winds that are due to low pressure systems passing north of the shelf. This includes Arctic-born

storms as well as Pacific-born storms, which temporarily displace the Beaufort High (Lukovich and Barber, 2006; Pickart et al., 2013; Dmitrenko et al. 2018; Foukal et al., 2019).

The observational knowledge to date of the circulation in Mackenzie Canyon is based on individual synoptic shipboard sections and a small number of moorings, both of which have been inadequate to resolve the flow components in and near the canyon. In this study we analyze data from a cross-shelf/slope array of five moorings that was deployed in 2016–17 in the vicinity of the canyon. This has provided the first opportunity to identify the different parts of the boundary current system from the inner shelf to the base of the slope year-round. The data reveal four distinct flow components, the nature of which are explored, including upstream/downstream connections, wind-forced variability, and impacts of sea ice. The paper is organized as follows. We begin with a description of the mooring data, followed by a presentation of the results. The year-long mean fields of velocity and hydrography are described first, followed by an investigation of the individual flow components on the shelf and upper slope, including their potential drivers. Lastly, we address the nature and forcing of the circulation at the base of the canyon and its connection to the Beaufort Gyre.

2. Data and methods

2.1. Mooring array

We use data from a mooring array deployed across the shelf and slope in the vicinity of Mackenzie Canyon (also referred to as Mackenzie Trough; Williams et al., 2006), in the Canadian Beaufort Sea (Fig. 1). The array consisted of five moorings named M0–M4, progressing onshore to offshore, deployed from October 2016 to September 2017 as part of Marine Arctic Ecosystem Study (MARES). A second deployment was carried out (moorings M1–M4 only), but, due to heavy ice conditions in fall 2018, one of the moorings could not be recovered until October 2019. Because of this delay, we report here on the first year of data only. The array design is presented in Fig. 2. The two shelf

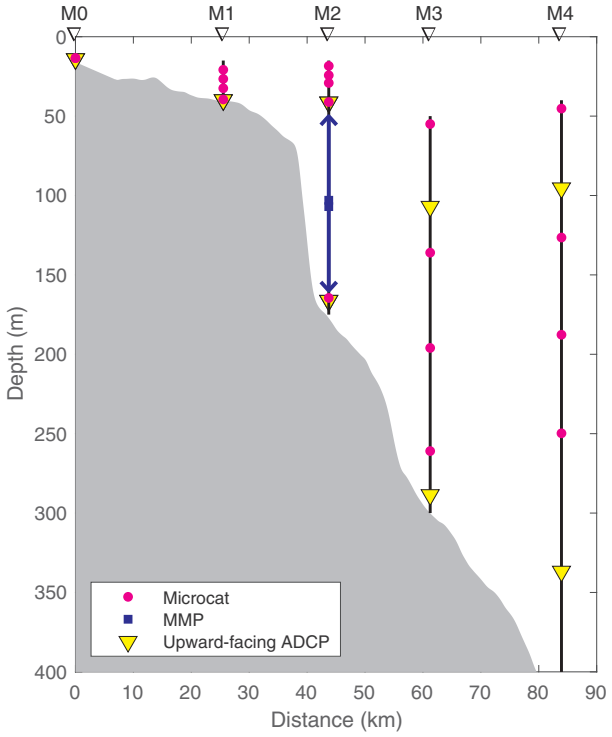

Fig. 2. Configuration of the mooring array in the vertical plane. The legend shows the different scientific instruments used: MicroCATs, a McLane moored profiler (MMP), and upward-facing acoustic Doppler current profilers (ADCPs).

moorings consisted of bottom-mounted frames, while the other three were tall moorings. All of the moorings contained MicroCATs for measuring pressure, temperature, and salinity, sampling every 30 min at M0 and every 15 min at M1–M4.

Moorings M1 and M2 included three MicroCATs extending into the upper part of the water column typically impacted by ice keels. These were attached to the main part of the mooring using a series of weak links and low-drag floats, and the data were inductively transferred to a logger at depth. The idea was that if the top float became snagged by ice – which was deemed a real possibility – it would break free, and the upper-most MicroCAT would drop to a deeper depth beneath the next float. If the second float were subsequently impacted, then the weak link on the main part of the mooring was designed to break so that the entire mooring would not be dragged. In this scenario all three instruments would be lost, but the data obtained up to that point would be saved on the logger. As it turned out, both of the top instruments were impacted by ice. The pressure sensors revealed that the shallowest MicroCAT on M2 fell down from 20 m to 30 m on 10 March 2017, while that on M1 dropped from 18 m to 26 m ten days later. The configuration of MicroCATs remained this way for the duration of the deployment, implying that there were no further ice encounters. Overall, the data return on the MicroCATs was 100%.

In addition to the point hydrographic measurements, mooring M2 included a McLane moored profiler (MMP) to collect vertical profiles of temperature and salinity between 50 and 155 m depth (Fig. 2). The MMP sampled 6 times per day, where each profile took approximately 4 min to complete. The data return was excellent, except during the month of August 2017 where there were a significant number of missing profiles. Hourly vertical sections of the hydrographic variables (potential temperature, salinity, potential density) were constructed using Laplacian-Spline interpolation with a grid spacing of 5 km in the horizontal and 5 m in the vertical.

Velocities were measured using upward-facing acoustic Doppler current profilers (ADCPs) with vertical resolutions ranging from 0.5 to 8 m and sampling intervals ranging from 20 to 60 min (see Table 1). Prior to the deployment of the array, the ADCP compasses were calibrated on nearby Herschel Island (see Fig. 1b), far from any sources of ferromagnetism. After completion of the post-cruise data processing, the velocity timeseries were de-tided using the T_Tide harmonic analysis toolbox (Pawlowicz et al., 2002). The profiling range for each mooring is listed in Table 1. The ADCP data return was 100% at moorings M1–M4, but the instrument at M0 stopped working at the beginning of August 2017. Velocities were rotated into alongstream and cross-stream components at each mooring (see Table 1 for the alongstream angles), and hourly vertical sections were constructed. Ice velocity was also measured at each mooring, with the exception of M0.

2.2. Atmospheric data

We use hourly wind data from the meteorological station on Herschel Island (Fig. 1b), which is the nearest weather station to the mooring array. The data were obtained from Environment Canada (https://weather.gc.ca/). To address the large-scale atmospheric conditions, we employed the ERA5 reanalysis wind product (Hersbach, 2018) from the European Center for Medium-Range Weather Forecasts (ECMWF, https://www.ecmwf.int/). ERA5 is an updated version of ERA-Interim with higher spatial and temporal resolution (0.25° and 3 h), and has been used in multiple studies (Berrisford et al., 2009). The ERA5 wind timeseries for the grid point closest to Herschel Island agrees well with the weather station data, attesting to the accuracy of the reanalysis data (the Herschel Island data are not assimilated into ERA5).

2.3. Satellite data

The daily ice concentration data used in the study are provided by

Table 1
Information for the ADCPs at each mooring.

Mooring ID	Bottom depth (m)	Velocity instruments	Instrument depth (m)	Depth range of profiling (m)	Vertical resolution (m)	Sample interval (minutes)	Along-isobath direction (°T)
M0	14	1000 kHz Nortek AD2CP	14	0.7–13.2	0.5	60	98.5
M1	40	300 kHz ADCP	39	3.5–35.5	2	30	123.2
M2	175	300 kHz ADCP	35	5.0–154.5	2	30	145.0
		300 kHz ADCP	162		4	30	
M3	300	150 kHz ADCP	150	11.0–260.0	2	20	138.9
		75 kHz ADCP	280		8	20	
M4	440	150 kHz ADCP	100	10.0–310.0	2	20	76.6
		75 kHz ADCP	330		8	20	

the Remote Sensing of Sea Ice Research Group at the University of Bremen (https://seaice.uni-bremen.de/). The data are obtained by applying the ARTIST (Arctic Radiation and Turbulence Interaction STudy) Sea Ice algorithm (Spreen et al., 2008) to the original measurements of the new Advanced Microwave Scanning Radiometer (AMSR2, the successor of AMSR-E) launched in 2012 (Beitsch et al., 2014). The resolution of the product is 3.125 km in our study region, which allows us to resolve the ice concentration at each of the mooring sites.

Part of the analysis carried out in the study makes use of the surface geostrophic velocity product distributed by the Copernicus Marine and Environment Monitoring Service (CMEMS, http://www.marine.copernicus.eu). This daily gridded product has a spatial resolution of 0.25°, and is based on information from multiple altimeter missions, e.g. Topex/Poseidon and the Jason series. Here we use the delayed-time version that has been reprocessed with enhanced quality control and interpolation.

3. Velocity and hydrographic structure

3.1. Mean state

We begin by presenting the year-long mean structure of the velocity across the mooring array. Fig. 3a shows the depth-averaged velocity vectors (upper 260 m) along with the standard error ellipses at each site. This reveals a complex current system associated with Mackenzie Canyon. On the inner shelf, the mean flow at M0 parallels the coast to the east towards Herschel Island. Farther offshore, on the outer shelf, the flow at M1 is much stronger (> 0.1 m s^{-1}) but is directed to the northwest, opposite to that on the inner shelf. Seaward of the shelfbreak the mean flow at M2 is not significantly different than zero. However, there is large vertical shear at this location (Fig. 3b): the mean flow in upper 40 m is oppositely directed to the mean flow in the layer below. This is addressed further in Section 3.2. At the two deepest sites the flow at M3 is to the southeast (up-canyon), while the flow at M4 is to the southwest, both with comparable magnitude. This is true as well for the upper and lower layer-mean flows (Fig. 3b). To define the alongstream and cross-stream directions at each site, we used the orientation of the standard error ellipses. In particular, the orientation of the major axis of the ellipse is taken to be the alongstream direction (positive eastward), while the orientation of the minor axis is the cross-stream direction (positive offshore). With the exception of M2, which has an insignificant depth-mean flow, the alongstream directions so defined are close to the directions of the mean vectors.

To show the depth dependence of the flow, we computed the year-long mean vertical section of alongstream velocity (Fig. 4a). This reveals a strong, surface-intensified westward flow in the upper 50 m centered at mooring M1. We refer to this as the shelf current, which is much stronger than the weak barotropic flow adjacent to the coast. The velocity at M2 on the upper slope has a three-layer structure: westward flow near the surface and bottom, and eastward flow at mid-depth. This is the reason for the weak depth-averaged vector at that site (Fig. 3a). Farther down the slope, the alongstream flow has a dipole-like structure with equal but opposite mid-depth intensified flows (centered near 80 m depth) at M3 and at M4 within the canyon.

The year-long mean vertical sections of potential temperature, salinity, and potential density (Fig. 4) show that the shelf current

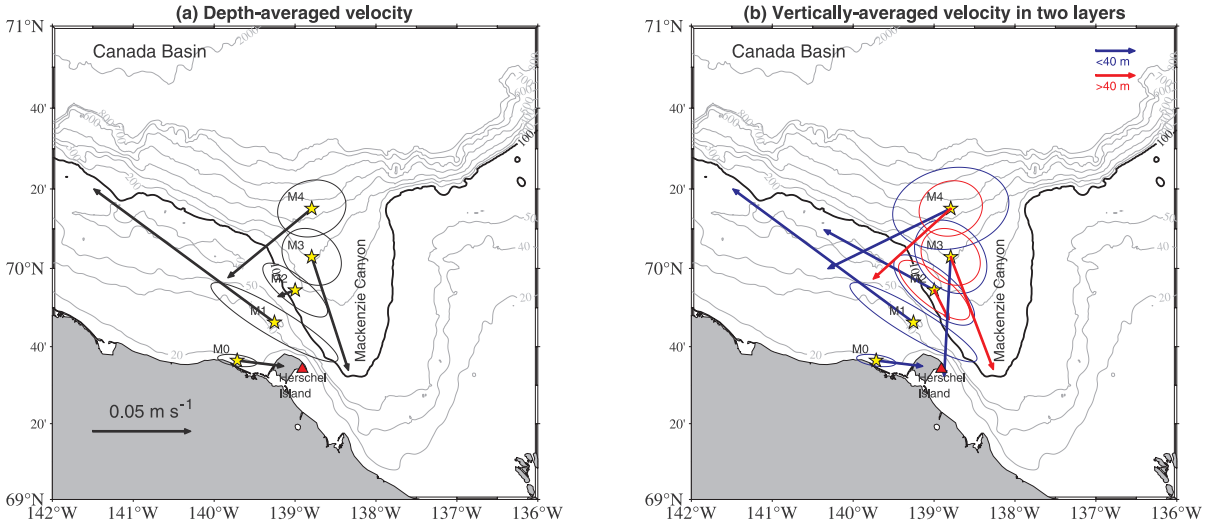

Fig. 3. Year-long mean vertically-averaged velocity vectors for (a) the full water column, and (b) the upper 40 m (blue vectors) and the layer below (red vectors), with the associated standard error ellipses. Bathymetry contours are in meters; the 100-m isobath at the rim of Mackenzie Canyon is highlighted by the thick contour. The red triangle marks the location of the Herschel Island meteorological station.

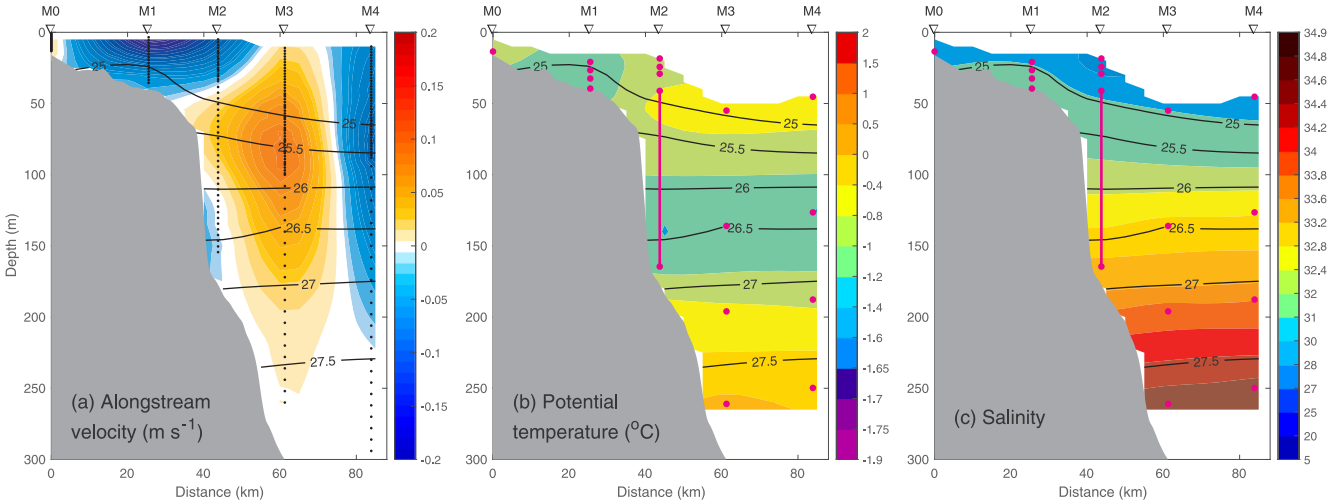

Fig. 4. Vertical sections of (a) year-long mean alongstream velocity (color), (b) potential temperature (color) and (c) salinity (color) overlain by mean potential density (contours, kg m^{-3}). The black dots in (a) are the ADCP data points. The magenta line in (b and c) denotes the vertical range of the MMP, and the magenta dots in (b and c) show the location of the MicroCATs. The bottom depth data are from the ship's echosounder.

advects relatively cold and fresh water (T < -1°C and S < 31) in the upper 30 m. The isopycnals slope upward onto the shelf, which is consistent with the surface-intensified flow. Seaward of the shelf current, the water in the upper-layer is warmer, while beneath this there is a layer of cold water sitting atop the warm Atlantic water at depth. We note that the coarse vertical resolution of the hydrographic measurements at the two offshore moorings (M3 and M4) makes it difficult to capture the detailed structure of the water characteristics and isopycnal slope in this region.

It is of interest to compare the water masses observed at the MARES array with those measured to the west in the Alaskan Beaufort Sea. Moorings have been maintained in the vicinity of the shelfbreak at 152°W (roughly 150 km to the east of Pt. Barrow) on and off since 2002 (see Fig. 1a). At this location most of the water is identifiable as Pacific-origin water advected by the shelfbreak jet. The two Pacific summer waters are: Alaskan Coastal Water (ACW), which is comprised of run-off from the Alaskan land mass (Weingartner et al., 2005), and Bering Summer Water (BSW), which is a mixture of warm Anadyr Water and Central Bering shelf Water (Coachman et al., 1975; Pisareva et al., 2015). The two Pacific winter waters are: Newly Ventilated Winter Water (NVWW), which is formed by convective overturning due to air-sea buoyancy loss in both the Bering and Chukchi Seas and is near the freezing point (Pickart et al., 2016), and Remnant Winter Water (RWW), which is NVWW that has been warmed due to solar radiation and/or mixing with warmer ambient waters (Gong and Pickart, 2016).

A volumetric potential temperature/salinity (θ/S) diagram is shown for the year 2016–17 in Fig. 5a for the core of the shelfbreak jet at 152°W. All of the Pacific-origin water masses are present, with the largest volume corresponding to the two winter water masses. There is also the signature of the warm, salty Atlantic Water (AW), which is the densest water measured. The cold, fresh water that is lighter than RWW is a mixture of sea ice melt water and meteoric water (referred to as MWM, which includes precipitation and river discharge).

The equivalent volumetric θ/S diagram for the year-long MARES data from the shelfbreak mooring (M2) is shown in Fig. 5b. To assure consistency between the two plots, we excluded the data shallower than 40 m from the MARES mooring. There are some notable differences between the two sites. Firstly, there was no ACW present at any time of the year at the MARES array, and only a tiny amount of BSW. This is in line with the rare occurrence of BSW on the Mackenzie shelf based on over three decades of data (H. Melling, pers. comm., 2019). The absence of a Pacific summer water signal is consistent with the energetics analysis of von Appen and Pickart (2012), which suggested that both of the summertime configurations of the Alaskan Beaufort shelfbreak jet should spin-down before reaching the Canadian Beaufort Sea. Secondly, there was a significant amount of MWM present at the MARES site with temperatures colder than 0 °C. Some of this is the signature of newly melted sea ice near the freezing point, but it is also likely that Mackenzie River water is included in the mixture due to wind mixing. Note that the small signal of BSW could reflect MWM-origin waters that have warmed during the summer.

Using the θ/S definitions in Fig. 5, we computed the percent presence of each water mass in the vertical plane using the full year of MARES data (Fig. 6). As noted above, there is no ACW present at the array, and only a very small amount of BSW which is found in the upper 50 m, mostly at the inner-shelf mooring. The inner-most site is also where the NVWW was measured, confined to the months of November-December 2016 (with a very small amount at the outer-shelf mooring). This is consistent with the notion that winter water is formed on the inner Beaufort shelf during freeze up (Jackson et al., 2015) and spreads offshore. RWW was the primary water mass present from about 70–200 m, which is true as well on the Alaskan Beaufort slope (Lin et al., 2016) and also on the Chukchi slope (Corlett and Pickart, 2017). Beneath this is the AW layer. Finally, the upper layer (shallower than about 70 m) contains mostly MWM.

3.2. Components of the boundary current system

The complex velocity structure revealed by the depth-mean vectors and the mean vertical section raises several questions regarding the boundary current system at this location. For instance, is there a signature of a year-round shelfbreak jet, such as that seen farther to the west in the Alaskan Beaufort Sea? What is the nature of the dipole-like circulation offshore within Mackenzie Canyon? To help identify the components of the boundary current system and the associated variability, we computed empirical orthogonal functions (EOFs) for the timeseries of vertical sections of the alongstream and cross-stream velocity. In the first mode (EOF1), accounting for 39% of the variance, the alongstream velocity variability is in phase across the shelf and slope, with a maximum signal at mooring M1 (Fig. 7a). This is clearly associated with the shelf current, the variability of which is discussed in Section 4. The second mode (EOF2), accounting for 11% of the variance (Fig. 8), shows a dipole-like structure in the alongstream velocity at the two offshore moorings that is very similar to the mean flow at these sites (compare Figs. 4a and 8a). This indicates that there is an in-phase, alternating flow at the outer part of the array that varies independently

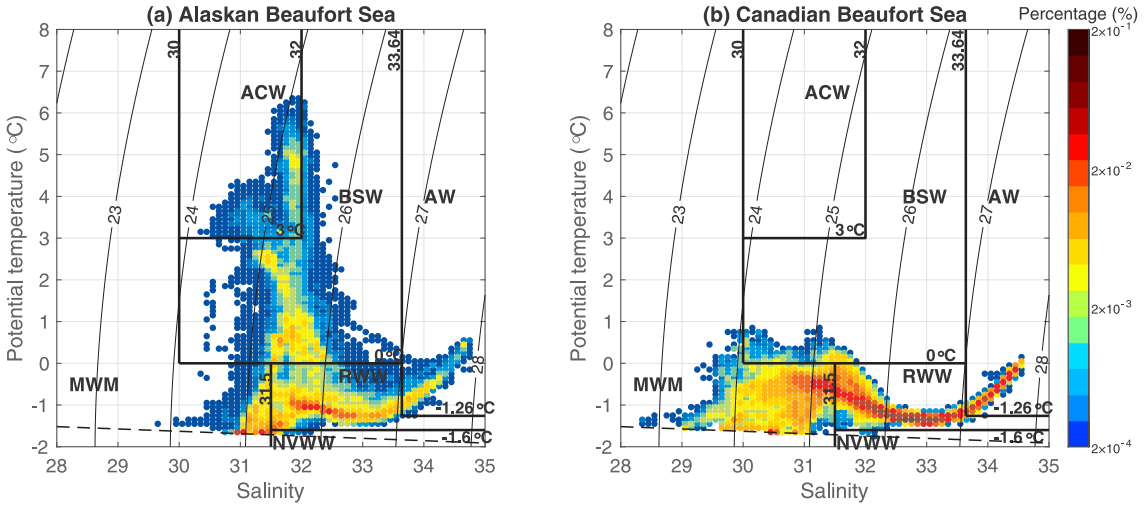

Fig. 5. Percent occurrence of θ/S values using the mooring data at the core of shelfbreak jet (a) in the Alaskan Beaufort Sea and (b) in the Canadian Beaufort Sea (M2) during 2016–17. ACW = Alaskan coastal water; BSW = Bering summer water; NVWW = newly ventilated winter water; RWW = remnant winter water; AW = Atlantic water; and MWM = sea ice melt water / meteoric water.

of the shelf current. We argue that this is a recirculation within the canyon, the nature and variability of which are investigated in Section 5.

Note that the signature of EOF1 in alongstream velocity extends to depths > 100 m seaward of the shelfbreak. This is the part of the water column where the shelfbreak jet is present in the Alaskan Beaufort Sea. In an effort to bring out the signature of such a flow at the MARES array, we did a simple calculation to remove the recirculation.

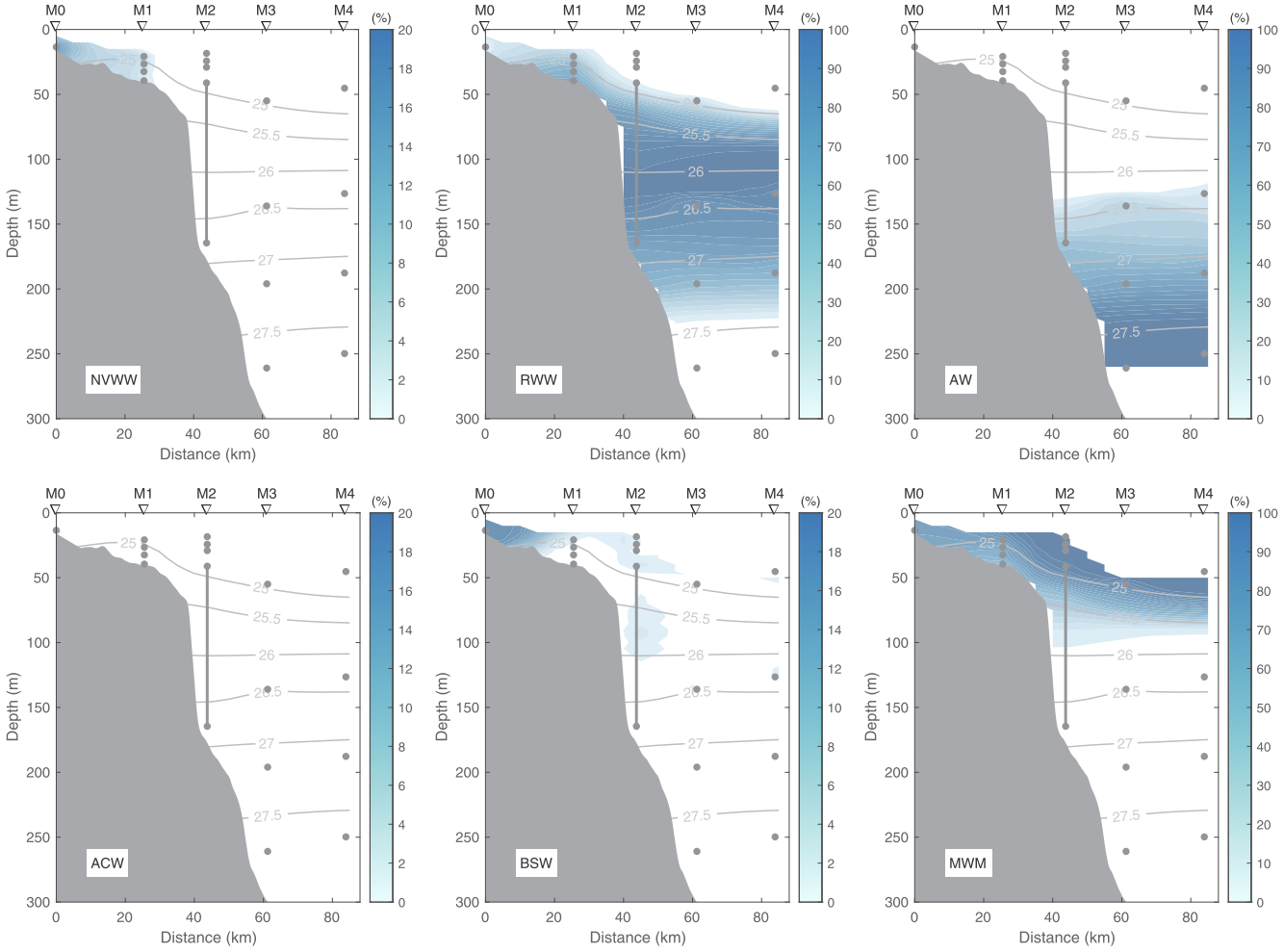

Fig. 6. Vertical sections of the mean percent occurrence of the water masses in at the MARES array over the course of the year (see Fig. 5 for the water mass definitions).

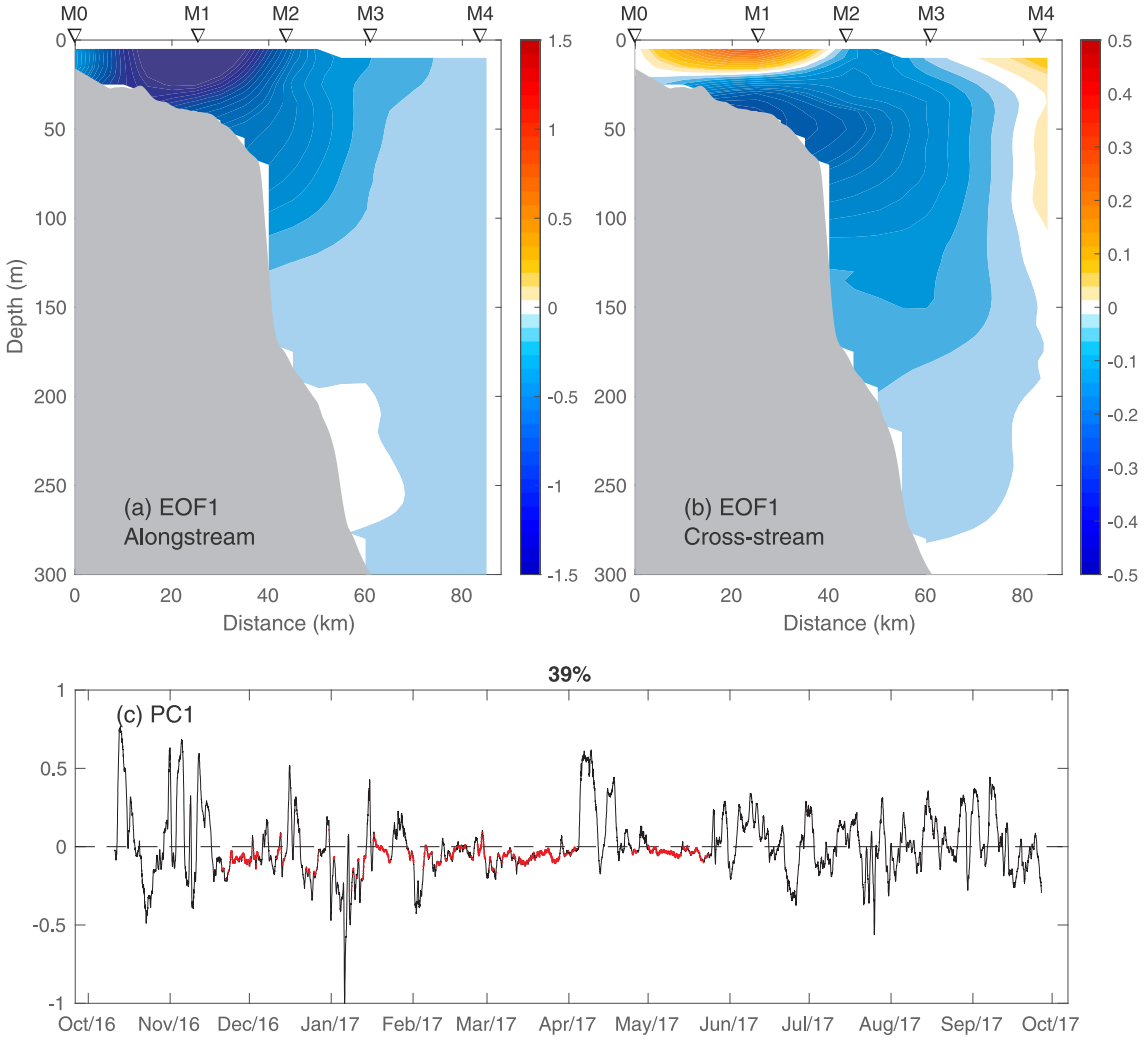

Fig. 7. Empirical orthogonal function (EOF) mode 1 for (a) the alongstream velocity and (b) the cross-stream velocity. (c) The associated principal component timeseries, where the red portions indicate the periods of nearly-immobile ice at mooring M1. The percent variance explained by the mode is indicated at the top.

Assuming that the recirculation is balanced at the two offshore mooring sites, we subtracted the vector velocity at M4 from that at M3 and M4 for each depth and timestep. The resulting mean vertical sections of alongstream and cross-stream velocity with the recirculation removed are shown in Fig. 9. The eastward-flowing shelfbreak jet is now evident as a bottom-intensified flow, as it is in the year-long mean state in the Alaskan Beaufort Sea (Nikolopoulos et al., 2009; Lin et al., 2016; Foukal et al., 2019).

Our results demonstrate that the boundary current system at the location of the MARES array consists of the following components: a coastal flow, a shelf current, a shelfbreak jet, and an offshore recirculation. We now address the first three components, followed by the offshore recirculation.

4. Currents in the vicinity of the shelfbreak

4.1. Seasonality of transports

The cross-sectional area of the shelf current and shelfbreak jet were defined by the velocity contour corresponding to 10% of the peak value for each current in the mean section (the dashed lines in Fig. 9a). As noted above, the ADCP record at the inner-shelf mooring M0 ended two months before the other records. Since the shelf current is largely symmetric around mooring M1 (the gridded section implies that the shelf current extends close to mooring M0), we simply doubled the transport measured by moorings M1 and M2 during this two-month period.

The monthly mean transport timeseries of both currents are shown in Fig. 9c. The transport of the shelf current was westward for most of the year except for the months of January through March when it was weakly eastward or indistinguishable from zero. The largest transport occurred in April, -0.35 Sv, during an extended period in which the sea ice concentration was largely diminished, allowing a greater water column response to the wind. During the warm months of the year (May–September) the transport was relatively constant, -0.15 Sv. October stands out in that the mean value is large, -0.23 Sv, and there was also large variability. The year-long mean transport of the shelf current was -0.12 ± 0.03 Sv. The transport of the shelfbreak jet was consistently weaker than that of the shelf current; its year-long mean value was 0.03 ± 0.02 Sv directed to the east. The seasonal variability of the flow was also smaller than that of the shelf current. Most of the year the transport was close to zero (weakly positive or negative), except for the months of June, October, and December when the transport was > 0.1 Sv.

We can compare the transport of the shelfbreak jet to that measured over the same time period upstream in the Alaskan Beaufort Sea at the 152°W mooring. Using the proxy developed by Brugler et al. (2014), the mean volume flux is estimated to be 0.08 ± 0.02 Sv. As noted above, the dearth of Pacific summer water at the MARES site, together with the energetics analysis of von Appen and Pickart (2012), suggests that

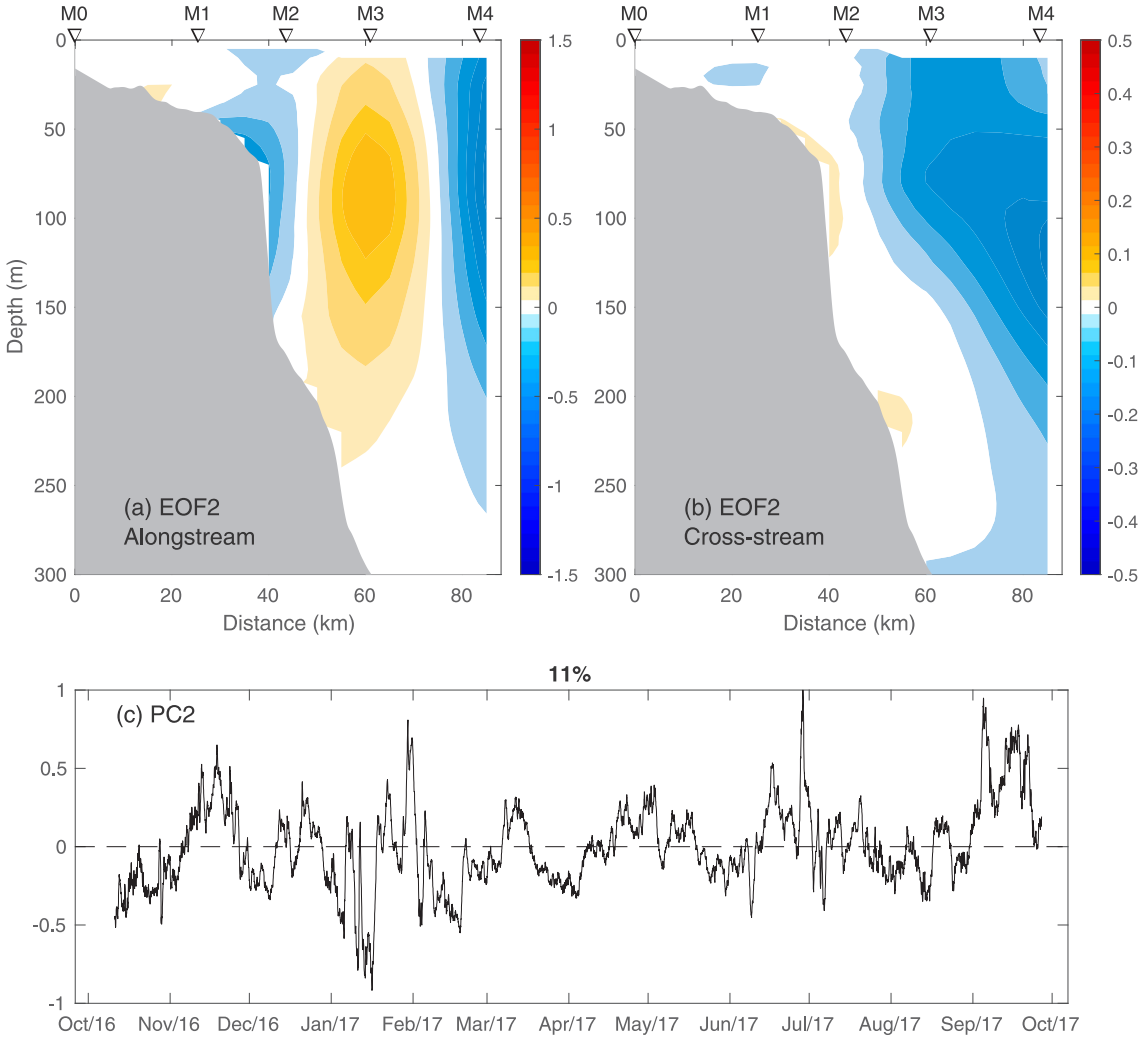

Fig. 8. Same as Fig. 7 except for EOF mode 2.

much of the Alaskan Coastal Current contribution to the shelfbreak jet does not make it to the Canadian Beaufort Sea. This is consistent with the reduction in transport between the two sites and the fact that the shelfbreak jet is not surface-intensified in the summer months at the MARES site, as it is in upstream.

To quantify the relationship between the two locations, we computed the lag-correlation between the 10-day low-passed transport timeseries, which shows two statistically significant peaks (Fig. 10a; the result is not sensitive to the width of the lowpass filter). The first peak is at 55 hr, and in Fig. 10b we have shifted the timeseries at the MARES site ahead by this amount, which shows good agreement between the two timeseries. Based on the distance between the two sites (530 km), this results in a propagation speed of 2.7 m s^{-1}. This is close to the propagation speed of velocity fluctuations observed by Aagaard and Roach (1990) for two moorings along the Alaskan Beaufort shelf edge (2.3 m s^{-1}). They attributed this to eastward propagating shelf waves, which is in line with the model results of Pickart et al. (2011) who showed that barotropic shelf waves travel at this speed in the Beaufort Sea. The second peak in correlation in Fig. 10a is at 779 hr, or 32.5 days. This results in a speed of 0.2 m s^{-1}, which is consistent with the typical advective speed of the shelfbreak jet in Alaskan Beaufort Sea (Lin et al., 2016). Our results suggest then that, although there is a reduction in transport as the shelfbreak jet flows eastward, the variation in transport at MARES site is linked with that upstream via both shelf waves and advection.

4.2. Effect of wind

The cross-stream velocity component of EOF1 consists of oppositely-directed flow over the shelf, with the zero crossing near 20 m (Fig. 7b). This is indicative of an Ekman cell and suggests that EOF1 mainly captures wind-driven circulation. As discussed above, the along-stream velocity component of EOF1 shows that this mode is clearly associated with the shelf current, but the signature of the mode extends to the depth of the shelfbreak jet as well at mooring M2 (Fig. 7a). This implies that both currents are impacted by the wind. To investigate the role of the wind we use the along-coast component of the wind timeseries from the Herschel Island weather station. The orientation of the coastline is also the direction of the major axis of variance of the wind velocity (127°T, positive eastward).

As demonstrated in previous studies of upwelling and downwelling in the Alaskan Beaufort Sea, the boundary current has a clear wind-driven response as long as the ice is mobile (Schulze and Pickart, 2012; Foukal et al., 2019). Ice velocity can be greatly reduced by strong internal ice stress, and, in the limit, sea ice becomes nearly-immobile – in which case we don't expect to see a direct relationship between the wind and currents. Here we use a threshold of ice velocity $<$ 0.03 m s^{-1} and ice concentration $>$ 95% to denote nearly-immobile ice conditions. Fig. 11a marks the periods of nearly-immobile ice for mooring M1 based on these criteria (yellow bands in the figure). Excluding these periods, the principle component timeseries (PC1) for EOF1 is significantly correlated with the along-coast wind velocity

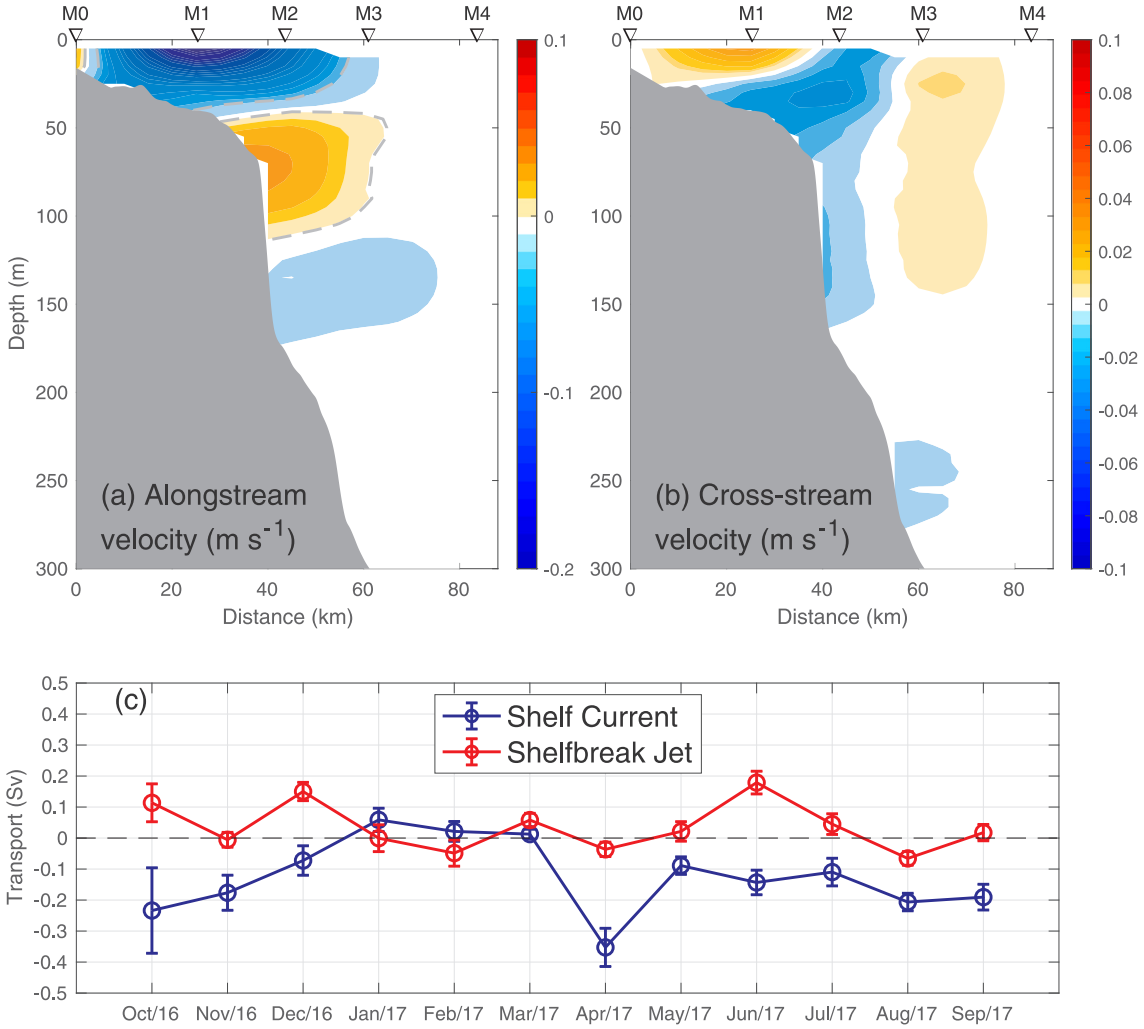

Fig. 9. Vertical sections of year-long mean (a) alongstream and (b) cross-stream velocity after removing the recirculation signal at moorings M3 and M4 (see text). The dashed contours in (a) mark the extent of the shelf current and shelfbreak jet, defined by the velocity corresponding to 10% of the peak value for each current. (c) Monthly mean transport of the shelf current and shelfbreak jet. The standard errors are included. Positive values are eastward.

(Fig. 11b). We have low-passed both timeseries in Fig. 11b with a 2-day filter to remove high-frequency variability.

To quantify the relationship between the wind and circulation, we reconstructed the mode 1 alongstream and cross-stream velocity fields using the EOF1 and PC1 timeseries added back into the mean. As an example of the mode 1 structure, Fig. 12 shows the positive and negative states of alongstream and cross-stream velocity for a ± 1 standard deviation of PC1. In the positive state (Fig. 12 top), the shelf current is strong and the shelfbreak jet is reversed, and there is an upwelling-favorable cross-stream Ekman cell. In the negative state

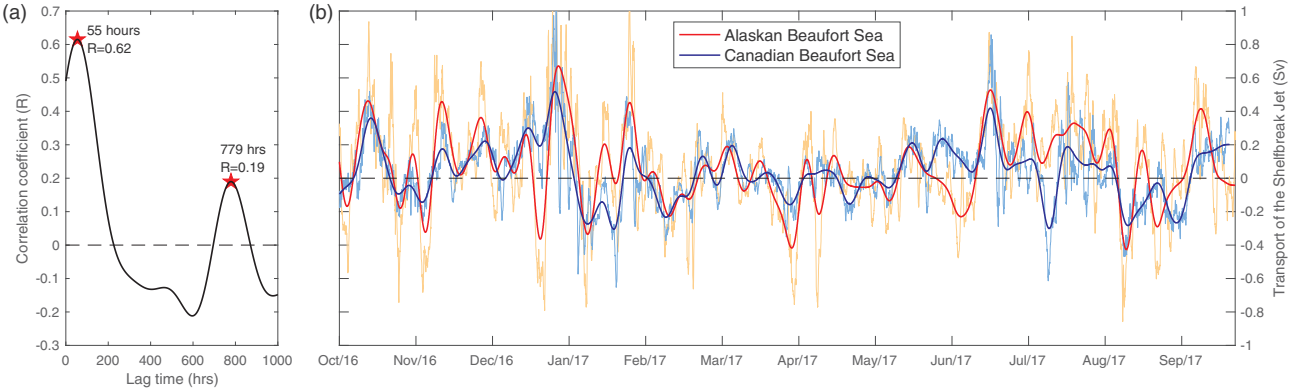

Fig. 10. (a) Lag-correlations between the 10-day low-passed shelfbreak jet transport in the Alaskan Beaufort Sea and Canadian Beaufort Sea in 2016–17. The two peaks in correlation coefficient are marked by the red stars. (b) The timeseries of transport in the Alaskan Beaufort Sea (red curve), and Canadian Beaufort Sea (blue curve), where the latter has been shifted forward by 55 h (the time lag of the peak correlation in (a)). The non low-passed timeseries are the thin curves, and the low-passed timeseries are the thick curves.

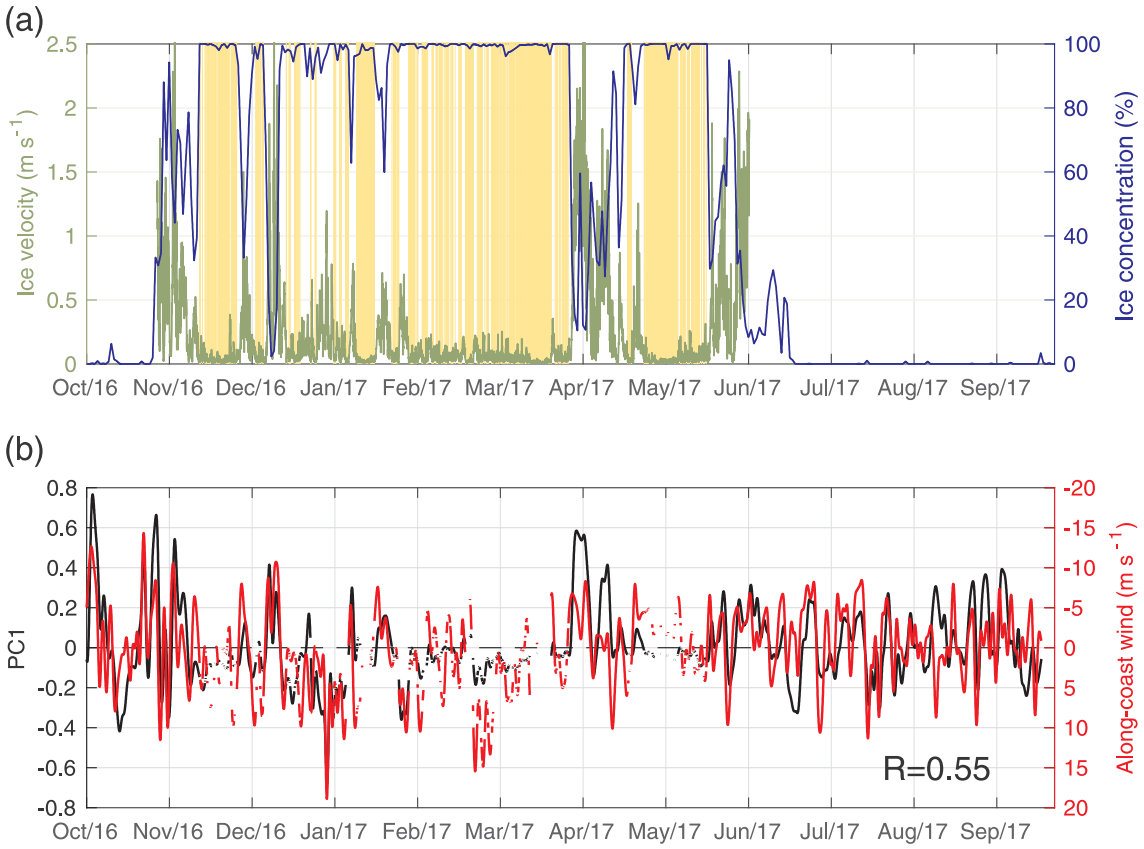

Fig. 11. (a) Timeseries of ice velocity (m s^{-1}, green) and ice concentration (blue) for mooring M1. The nearly-immobile ice periods are indicated by the yellow bands. (b) Two-day low-passed timeseries of the principle component of EOF1 (black) and the along-coast wind speed (red). The wind data are removed during nearly-immobile ice periods corresponding to (a).

(Fig. 12 bottom), the shelfbreak jet is strong and the shelf current is reversed, which is associated with a downwelling-favorable Ekman cell. We find that the re-constructed shelf current volume transport accounts for 97.5% of the variance of the full measured value. It is thus clear that the shelf current is predominantly wind-driven. For the shelfbreak jet the corresponding percentage is 21.8%, indicating that the variability of this current is only partially due to the wind – the inference being that upstream conditions (from the Alaskan Beaufort Sea) dictate much of the temporal variation, consistent with Fig. 10.

4.3. Role of ice

In the presence of mobile ice, the surface stress imparted to the ocean is a combination of wind stress and ice-ocean stress (e.g. Yang, 2006). It has been demonstrated in the Alaskan Beaufort Sea that the wind-driven upwelling and downwelling response is enhanced when there is a partial ice cover (Schulze and Pickart, 2012; Foukal et al., 2019), due to the effectiveness of ice keels in transferring momentum to the water column (Pite et al., 1995). This has been shown numerically as well (Martin et al., 2014). Using timeseries of ice velocity and near-surface velocity, Pickart et al. (2013) estimated the ice-ocean stress during an upwelling event at the 152°W site and found good agreement between the predicted Ekman response based on the total surface stress, and that measured using the moorings. However, this was a particularly energetic event with a large signal-to-noise ratio, and, as discussed in Williams et al. (2006) and Williams and Carmack (2008), it is generally difficult to accurately calculate ice-ocean stress using ADCP data. This is exacerbated by the fact that the drag coefficient depends on many factors, including ice roughness and concentration, and ocean stratification (McPhee, 2002). In the case of the MARES data, we were unable to produce reliable estimates of the ice-ocean stress.

Instead, we explore the relationship between ice concentration, ocean velocity, and wind for the shelf current. The ice concentration timeseries at mooring M1 (in the core of the shelf current) shows that the ice season lasts over half the year (Fig. 11a), and, during this time, the ice is nearly immobile roughly 18% of the time. During these periods, the PC1 timeseries hovers around zero (Fig. 7c). This is to be expected in that EOF1, which is primarily wind-driven, does not have any expression when the water column is shielded by an ice cover that is nearly stationary. As such, we exclude these periods from the present analysis.

Fig. 13a shows how the depth-averaged alongstream velocity at mooring M1 varies as a function of wind speed and ice cover (for mobile ice). One sees that the velocity is stronger when there is partial ice cover as opposed to periods of open water or highly concentrated ice. To isolate the effect of ice, we averaged the alongstream velocity for each bin of ice concentration. This shows that, for a given wind speed, the current is intensified when ice concentration is in the range of 20%–60% (Fig. 13b). This is consistent with the studies cited above showing that upwelling and downwelling are enhanced when there is partial ice cover. Conversely, to isolate the effect of wind, we averaged the alongstream velocity for each bin of wind speed (Fig. 10c, black curve). Not surprisingly, this reveals a trend of increasing alongstream velocity as the wind strengthens (although there are no data for extremely strong winds over 15 m s^{-1}). The sensitivity to wind is enhanced for open water versus full ice (concentration $>$ 95%), particularly for wind speeds exceeding 10 m s^{-1} (Fig. 13c, open circles).

It is worth noting that the alongstream flow at the inner shelf mooring M0 is also correlated with the along-coast wind (not shown, although it is evident in the first EOF mode for alongstream velocity; Figs. 7a and 12). In the mean, however, the coastal flow is directed to the east, while the wind-driven shelf current is westward (Fig. 3). This

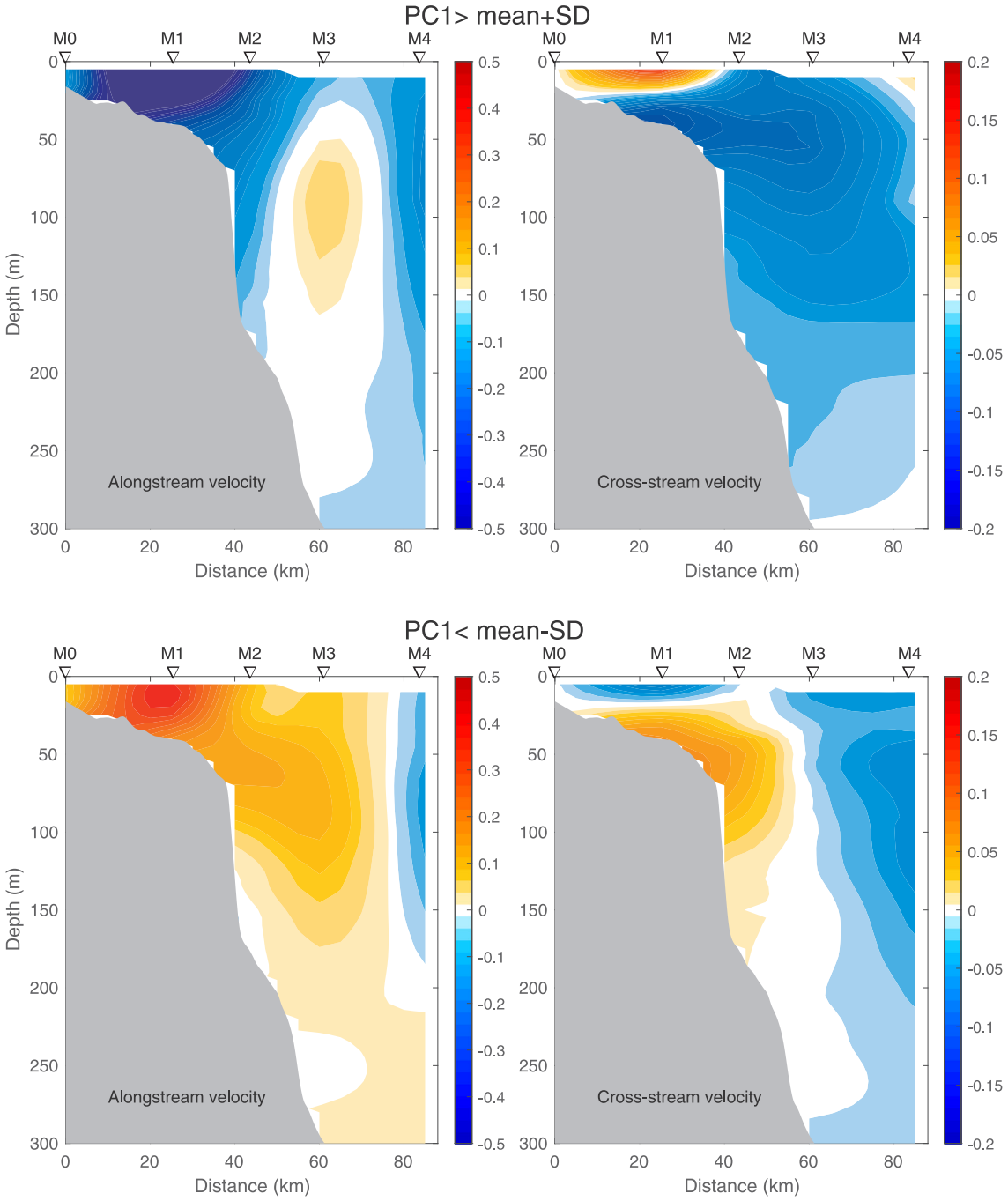

Fig. 12. Reconstructed alongstream and cross-stream velocity sections for opposite states of EOF1: (top) PC1 larger than the mean value plus the standard deviation; (bottom) PC1 less than the mean value minus the standard deviation.

discrepancy can be largely explained by the difference in ice cover between the M0 and M1 mooring sites. In particular, there were more extensive periods of nearly-immobile ice at the inner-shelf site, shortening the period of wind influence (only 2 out of 10 months). This resulted in comparatively more time that the site was subject to westerly or weak winds. During the ice-covered season (mid-November to the end of June), the flow at M0 was eastward with a velocity < 0.05 m s^{-1}. Over this period of time the variation of the velocity is not significantly correlated with the along-coast wind. This is consistent with observations on the Alaskan Beaufort inner shelf presented by Weingartner et al. (2017). Their data reveal that the under-ice flow is not maintained by wind, but varies linearly with the along-shore pressure gradient. Another potential mechanism is identified in the numerical study of Kasper and Weingartner (2012). They showed that upwelling-favorable wind decreases the sea level seaward of the ice edge, which results in a northward pressure gradient that can drive eastward geostrophic flow under the ice. This could also be occurring to some degree at mooring M0.

5. Recirculation in the canyon

5.1. Basic characteristics and dynamics

We now investigate the nature and cause of the middepth-intensified recirculation in the canyon that is evident in the mean velocity fields (Figs. 3 and 4a) and whose variability is captured by EOF2

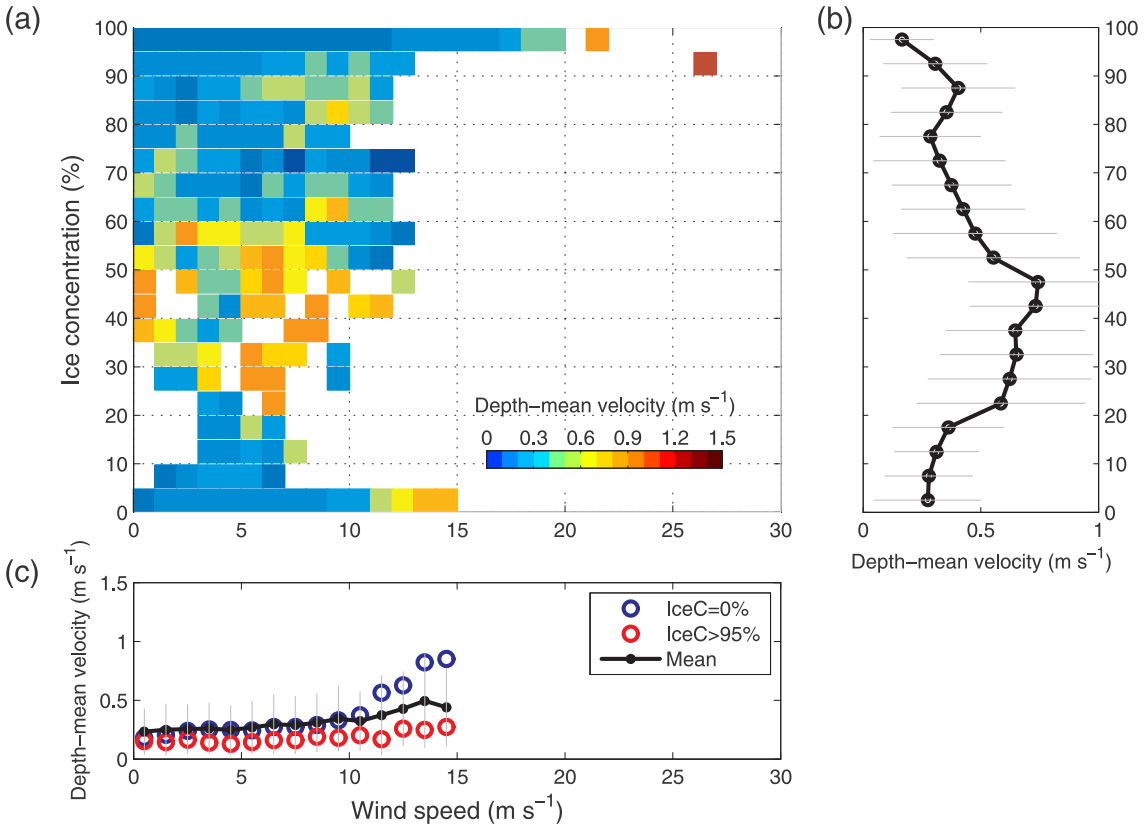

Fig. 13. (a) Ice concentration-wind speed diagram colored by the depth-mean alongstream velocity at M1. (b) The depth-mean velocity averaged across all wind speeds for each bin of ice concentration. Standard deviations are included (grey bars). (c) The depth-mean alongstream velocity averaged across all values of ice concentration for each bin of wind speed (black curve). Standard deviations are included (grey bars). The blue circles are for open water, and the red circles are for full ice (> 95%).

(Fig. 8). Recall that this mode only accounts for 11% of the variance. We also computed the EOFs using only the data from the two offshore moorings (M3 and M4). In this case the dominant mode consisted of an analogous dipole-like structure in the alongstream velocity accounting for 46% of the variance. The associated PC timeseries is highly correlated with the PC2 timeseries of the full array. Thus, we are confident in our assertion that EOF2 represents the recirculation. The cross-stream component of EOF2 shows that when the recirculation is strong, there is enhanced up-canyon flow (Fig. 8b). One then wonders if there is ambient flow from outside the canyon that is periodically getting diverted up the canyon.

The dynamics of cross-isobath circulation in a canyon is largely dictated by the canyon width and the water column stratification (e.g. Klinck, 1996; Hickey, 1997; Williams et al., 2006; Allen and Durrieu de Madron, 2009). To quantify the sensitivity to these two factors, Hyun (2004) set up a three-dimensional ocean circulation model with an idealized submarine canyon cutting across a shelf, perpendicular to an imposed along-shelf current approaching the canyon. Different numerical experiments were carried out in which the canyon width was varied while the stratification was held constant, and, conversely, in which the stratification was changed while the canyon width was kept the same. The stratification was cast in terms of the internal Rossby radius of deformation, $R = NH/f$, where H is the depth scale, f is the Coriolis parameter, $N = \sqrt{-\frac{g}{\rho_0}\frac{\partial \rho}{\partial z}}$ is the buoyancy frequency, g is the gravitational acceleration, ρ_0 is the reference density, andρ is the depth-dependent potential density. The results suggest that canyons can be classified as dynamically wide when the canyon width, W, is more than twice the internal deformation radius, $W > 2R$; otherwise they are considered dynamically narrow. In the former case, the along-shelf current turns into the canyon at its upstream flank. In the latter case, the current feels the entire canyon and the turning point of the flow occurs at the downstream flank of the canyon.

We computed R using the MMP data at mooring M2 to determine the vertical gradient of density, and taking the depth scale H to be 200 m, which is the depth of the Pacific water layer. Averaged over the year, R is 15 km. Based on the 100 m isobath (highlighted in Fig. 1b), Mackenzie Canyon is roughly 65 km wide. Hence, $W > 2R$ and Mackenzie Canyon is classified as a dynamically wide canyon (consistent with the conclusions of Williams et al., 2006). Note in Fig. 1b that the canyon is asymmetric in that its eastern flank is much broader than its western flank. Mooring M4 is in fact located at the base of the eastern flank, while mooring M3 is located near the axis of the canyon. Thus, the cyclonic turning of the flow and resulting recirculation seen in the MARES data are consistent with what is expected for a westward-directed current impinging on dynamically wide canyon.

5.2. Potential drivers of the variation

In light of the above, if there is flow along the continental slope approaching the mouth of Mackenzie Canyon, at least part of it will be diverted up the canyon, across isobaths, resulting in a recirculation. What is the source of the westward-directed current? We surmise that it is the southern edge of the Beaufort Gyre. This becomes clearer when considering the variation in the recirculation measured by moorings M3 and M4.

Returning to EOF2, one sees that there is significant variability in the PC2 timeseries (Fig. 8c) on intra-seasonal timescales (periods of 30–60 days). Kulikov et al. (1998) analyzed velocity data from a set of sparsely spaced moorings along the continental slope of the Canadian Beaufort Sea, and found that this general frequency band accounted for 65% of the kinetic energy. They argued that the variability was tied to

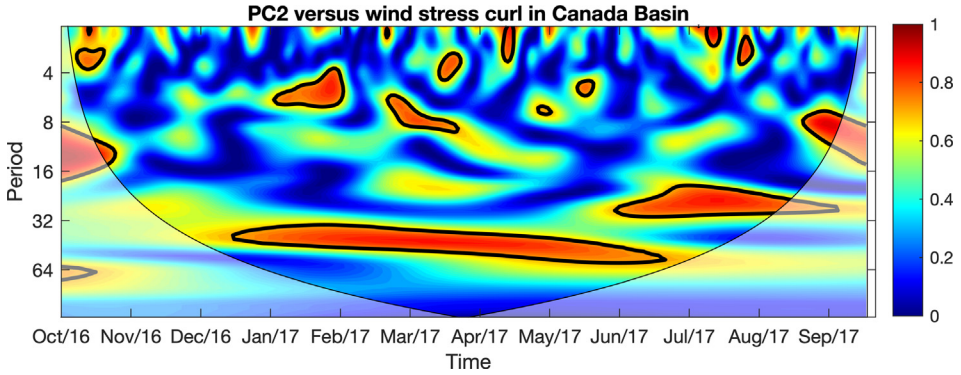

Fig. 14. Squared wavelet coherence between the principle component of EOF2 (PC2) and the wind stress curl in the Canada Basin. The wind stress curl is averaged over the region delimited by the dashed magenta box in Fig. 1a. Only the area outside of the white shading should be considered. The thick black contours represent the 95% confidence level.

the large-scale circulation. If this is associated with the southern edge of the Beaufort Gyre, then there should be link between the wind stress curl that drives the gyre and the time-varying strength of the canyon recirculation. To investigate this, we computed the wavelet coherence (Grinsted et al., 2004) between PC2 and the contemporaneous timeseries of wind stress curl averaged over the Canada Basin (Fig. 14). Note that the wavelet coherence is not a function of spectral power, but a generalized measure of correlation of two timeseries. The result reveals significant coherence between PC2 and the wind stress curl on intraseasonal timescales (30–60 days) throughout most of the year (there is large spectral power as well, not shown). Using the Herschel Island weather station data, we find no comparable year-long coherence between the along-coast wind and PC2 on any timescales.

To further elucidate this, we low-passed the timeseries of PC2 and the wind stress curl using a 25-day filter width (appropriate for intraseasonal timescales). The good agreement between the resulting timeseries confirms the link between the recirculation and wind stress curl forcing (Fig. 15). It still remains to be demonstrated, however, that the variability of the wind stress curl results in a time-varying westward flow along the continental slope that impinges on Mackenzie Canyon. We don't have coincident in-situ measurements of the flow to the east of the canyon during the MARES deployment period. However, there is information on the surface currents in this region during the open water period, derived from satellite-derived absolute dynamic topography (see Section 2.3). We averaged the surface geostrophic velocity within the dashed blue box outlined in Fig. 1a, upstream of Mackenzie Canyon. The result is shown in Fig. 15, demonstrating that the westward surface current co-varies with PC2 and the wind stress curl. In particular, the recirculation is stronger when the impinging zonal flow is stronger, driven by the wind-stress curl over the Canada Basin.

6. Discussion

We have argued that the recirculation measured by the two offshore moorings of the MARES array is due to a portion of the southern edge of the Beaufort Gyre being diverted up Mackenzie Canyon, due to dynamics associated with the canyon topography and water column stratification. The mooring array, however, is not able to capture the detailed circulation within the canyon. According to Hyun's (2004) numerical experiments, for a dynamically wide canyon the current recirculates cyclonically at the upstream flank, and subsequently bifurcates near the head of the canyon. One branch then flows back down the canyon along its downstream flank to rejoin the offshore zonal current, while the other branch flows in the upstream direction along a shallower isobath. The former pathway is consistent with the results of Williams et al. (2006). This pathway is also evident in the MARES data. Considering again the alongstream velocity structure of EOF2 (Fig. 8a), in addition to the dipole at moorings M3 and M4 there is a signal at M2 that varies oppositely to the inshore side of the recirculation. Adding EOF2 and PC2 back into the mean shows that, when the recirculation is strong, there is westward flow adjacent to the continental slope, extending down to 150 m (Fig. 16). We take this to be the downstream branch of the bifurcation. This westward flow also evident in the year-long mean velocity section, below the core of the shelfbreak jet (Figs. 4a and 9a).

The MARES measurements indicate that the recirculation in the canyon is middepth-intensified (Fig. 4a). This is in line with the numerical results of Klinck (1996) showing that the strongest diverted flow occurs at depths below the rim of the canyon. Overall, there are two potential factors influencing the vertical structure of the recirculation: local effects and upstream conditions. With regard to the former, Hickey (1997) found that the near-surface flow above the canyon rim is undisturbed by the canyon topography, while the cyclonic circulation occurs below this. In our case, the recirculation is clearly present in the surface layer, although weaker (Figs. 4a and 8a). This shallow manifestation is evident as well by the strong correlation between the strength of the recirculation measured at moorings M3 and M4 and the surface geostrophic velocity along the continental slope upstream of the canyon. With regard to upstream conditions, the vertical structure of the flow impinging on the canyon will likely influence

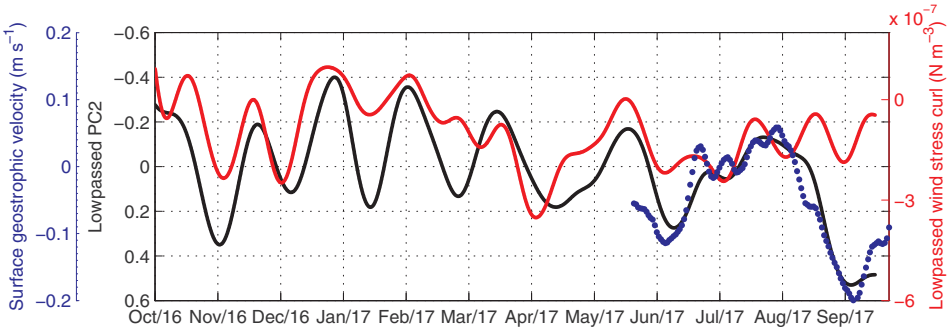

Fig. 15. Timeseries of 25-day low-passed PC2 (black curve), wind stress curl in the Canada Basin (red curve), and upstream zonal surface geostrophic velocity (blue dots). The latter two timeseries are averaged over the regions delimited by the magenta and blue dashed boxes in Fig. 1a, respectively.

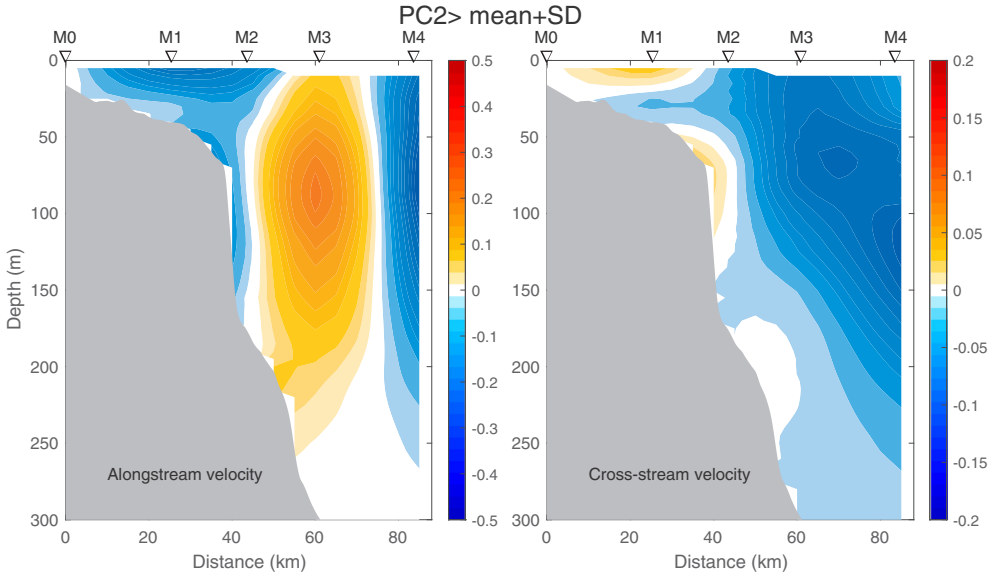

Fig. 16. Reconstructed alongstream and cross-stream velocity sections for positive states of EOF2 when PC2 is larger than the mean value plus the standard deviation.

the structure of the recirculation in the canyon. Based on previous mooring records from the continental slope to the east of Mackenzie Canyon, Forest et al. (2015) found that the mean westward flow was strongest at 100 m depth. Hence, the flow entering Mackenzie canyon should already be middepth-intensified.

7. Conclusions

In this study we have used data from a mooring array deployed across the shelf and slope in the Canadian Beaufort Sea from 2016 to 17 to clarify the circulation in the vicinity of Mackenzie Canyon, its response to wind and ice, and what role the topography plays. Based on the mean velocity vectors and vertical sections, together with an EOF analysis, we determined that there are four components comprising the boundary current system here: a coastal flow, a shelf current, a shelfbreak jet, and a recirculation in the canyon. These are depicted schematically in Fig. 17. We focused mainly on the latter three components.

In the mean, the shelf current is surface-intensified and flows towards the west with a transport of -0.12 ± 0.03 Sv. The cross-stream Ekman cell revealed by EOF1, and the good agreement between PC1 and the along-coast wind, indicate that the current is largely wind driven outside of periods of nearly-immobile ice cover. The reconstructed alongstream velocity of EOF1 shows that the volume transport associated with this wind-driven mode accounts for 97.5% of the variance of the fully measured current. The wind-driven response is strongly modulated by ice cover. The depth-averaged alongstream flow is strongest when the ice concentration is between 20 and 60%, in line with previous results showing that mobile ice keels are very effective at transmitting surface stress to the water column. While the alongstream velocity increases with increasing along-coast wind speed, the trend is enhanced for open water and more modest when the ice concentration is $> 95\%$.

The shelfbreak jet flows to the east with a mean volume transport of 0.03 ± 0.02 Sv. This is less than the mean shelfbreak jet transport of 0.08 ± 0.02 Sv measured in the Alaskan Beaufort Sea over the same time period. This reduction is consistent with previous evidence suggesting that the summertime configuration of the jet should spin down before reaching the MARES site. The lack of Pacific-origin summer water at the MARES array supports this interpretation. Despite the transport loss, the temporal variation in shelfbreak jet transport at the MARES site is significantly correlated with that upstream in the Alaskan Beaufort Sea. Two correlation peaks, at 55 hr and 32.5 days, are associated with shelf waves and advection, respectively.

The recirculation within the canyon was captured by the two offshore moorings of the array. It is middepth-intensified and varies independently from the shelf current and shelfbreak jet. The presence and variability of the recirculation is consistent with previous modeling work showing that a current impinging on a dynamically wide canyon gets diverted up the canyon on its upstream flank and subsequently bifurcates after flowing into shallower water. The calculated size of the deformation radius based on the mooring data, compared to the width of Mackenzie Canyon, indicates that it is dynamically wide. We argue that a portion of the westward flow associated with the southern edge of the Beaufort Gyre gets diverted up the canyon, resulting in the recirculation. This is consistent with the fact that the strength of the recirculation is significantly correlated with the wind stress curl in the Canada Basin – which drives the gyre – on intra-seasonal timescales. Furthermore, the variation in surface geostrophic velocity to the east of the array varies in concert with the recirculation. While the MARES mooring array is unable to resolve the full structure of the recirculation, there is evidence of the westward branch of the bifurcation at the mooring immediately inshore of the recirculation. The schematic of Fig. 17 shows the likely flow pattern within the canyon. Future work will address the biological ramifications of the cross-isobath flow of the recirculation and its relationship to coastal wind-driven upwelling.

Declaration of Competing Interest

The authors declare that they have no known competing financial interests or personal relationships that could have appeared to influence the work reported in this paper.

Acknowledgements

The authors are indebted to Fisheries and Oceans Canada for building the logistics for MARES into the at-sea missions of the Integrated Beaufort Observatory. We are grateful to the captain and crew of the CCGS *Sir Wilfred Laurier* for ably deploying and recovering the MARES array. Marshall Swartz assisted with the cruise preparation logistics. We thank the two anonymous reviewers for their input which helped improve the paper. This project was funded by the US Bureau of Ocean Energy Management (BOEM), on behalf of the National Ocean Partnership Program. The Canadian contribution was supported by the Environmental Studies Research Fund (ESRF Project 2014-02N).

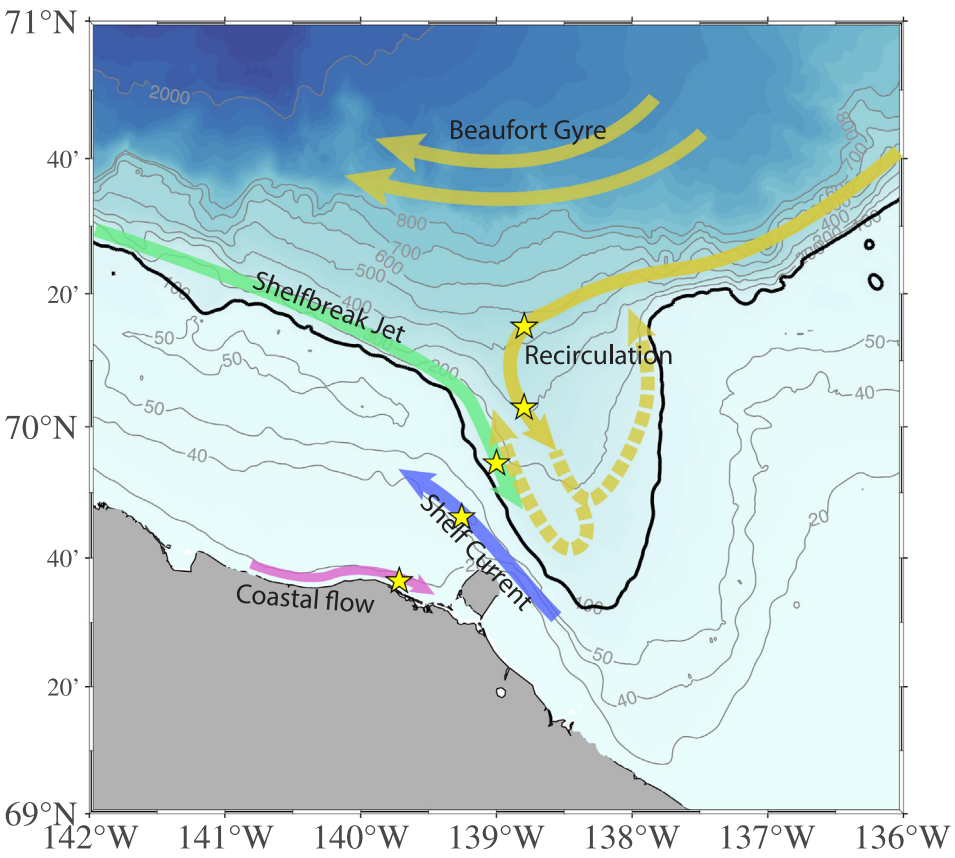

Fig. 17. Schematic circulation in the vicinity of Mackenzie Canyon, based on the MARES mooring data. The four components of the boundary current system are shown by different colored arrows: the coastal flow, shelf current, shelfbreak jet, and offshore recirculation. The main part of the Beaufort gyre is indicated as well. The dashed yellow arrows denote the deduced bifurcation following the results of Hyun (2004).

MARES publication 003.

References

Aagaard, K., Roach, A., 1990. Arctic ocean-shelf exchange: Measurements in Barrow Canyon. J. Geophys. Res. Oceans 95 (C10), 18163–18175.

Aagaard, K., Weingartner, T.J., Danielson, S.L., Woodgate, R.A., Johnson, G.C., Whitledge, T.E., 2006. Some controls on flow and salinity in Bering Strait. Geophys. Res. Lett. 33 (19).

Allen, S., Durrieu de Madron, X., 2009. A review of the role of submarine canyons in deep-ocean exchange with the shelf. Ocean Sci. 5 (4), 607–620.

Beitsch, A., Kaleschke, L., Kern, S., 2014. Investigating high-resolution AMSR2 sea ice concentrations during the February 2013 fracture event in the Beaufort Sea. Remote Sens. 6 (5), 3841–3856.

Berrisford, P., Dee, D., Fielding, K., Fuentes, M., Kallberg, P., Kobayashi, S., Uppala, S., 2009. The ERA-interim archive, ERA report series(1), 1–16.

Brugler, E.T., Pickart, R.S., Moore, G.W.K., Roberts, S., Weingartner, T.J., Statscewich, H., 2014. Seasonal to interannual variability of the Pacific water boundary current in the Beaufort Sea. Prog. Oceanogr. 127, 1–20. https://doi.org/10.1016/j.pocean.2014.05.002.

Coachman, L.K., Aagaard, K., Tripp, R., 1975. Bering Strait: the regional physical oceanography. University of Washington Press, Seattle.

Corlett, W.B., Pickart, R.S., 2017. The Chukchi slope current. Prog. Oceanogr. 153, 50–65.

Dmitrenko, I.A., Kirillov, S.A., Forest, A., Gratton, Y., Volkov, D.L., Williams, W.J., Lukovich, J.V., Belanger, C., Barber, D.G., 2016. Shelfbreak current over the Canadian Beaufort Sea continental slope: Wind-driven events in January 2005. J. Geophys. Res. Oceans 121 (4), 2447–2468.

Dmitrenko, I.A., Kirillov, S.A., Myers, P.G., Forest, A., Tremblay, B., Lukovich, J.V., Gratton, Y., Rysgaard, S., Barber, D.G., 2018. Wind-forced depth-dependent currents over the eastern Beaufort Sea continental slope: Implications for Pacific water transport. Elem. Sci. Anth. 6 (1).

Forest, A., Osborne, P.D., Fortier, L., Sampei, M., Lowings, M.G., 2015. Physical forcings and intense shelf–slope fluxes of particulate matter in the halocline waters of the Canadian Beaufort Sea during winter. Cont. Shelf Res. 101, 1–21.

Foukal, N.P., Pickart, R.S., Moore, G., Lin, P., 2019. Shelfbreak downwelling in the Alaskan Beaufort Sea. J. Geophys. Res. Oceans.

Gong, D., Pickart, R.S., 2015. Summertime circulation in the eastern Chukchi Sea. Deep Sea Res. II 118, 18–31.

Gong, Donglai, Pickart, Robert S., 2016. Early summer water mass transformation in the eastern Chukchi sea. Deep Sea Res. II 130, 43–55.

Grinsted, A., Moore, J.C., Jevrejeva, S., 2004. Application of the cross wavelet transform and wavelet coherence to geophysical time series. Nonlinear Processes Geophys. 11 (5/6), 561–566.

Hersbach, H., 2018. Operational global reanalysis: progress, future directions and synergies with NWP. European Centre for Medium Range Weather Forecasts.

Hickey, B.M., 1997. The response of a steep-sided, narrow canyon to time-variable wind forcing. J. Phys. Oceanogr. 27 (5), 697–726.

Hyun, K. -H. (2004), The effect of submarine canyon width and stratification on coastal circulation and across shelf exchange. Doctor of Philosophy (PhD), dissertation, Ocean/Earth/Atmos Sciences, Old Dominion University, DOI: 10.25777/76dbx339, https://digitalcommons.odu.edu/oeas_etds/57.

Itoh, M., Nishino, S., Kawaguchi, Y., Kikuchi, T., 2013. Barrow Canyon volume, heat, and freshwater fluxes revealed by long-term mooring observations between 2000 and 2008. J. Geophys. Res. Oceans 118 (9), 4363–4379.

Jackson, J.M., Melling, H., Lukovich, J.V., Fissel, D., Barber, D.G., 2015. Formation of winter water on the Canadian Beaufort shelf: New insight from observations during 2009–2011. J. Geophys. Res. Oceans 120 (6), 4090–4107.

Jones, E., Swift, J., Anderson, L., Lipizer, M., Civitarese, G., Falkner, K., Kattner, G., McLaughlin, F., 2003. Tracing Pacific water in the North Atlantic ocean. J. Geophys. Res. Oceans 108 (C4).

Kasper, J.L., Weingartner, T.J., 2012. Modeling winter circulation under landfast ice: The interaction of winds with landfast ice. J. Geophys. Res. Oceans 117 (C4).

Kirillov, S., Dmitrenko, I., Tremblay, B., Gratton, Y., Barber, D., Rysgaard, S., 2016. Upwelling of Atlantic Water along the Canadian Beaufort Sea continental slope: Favorable atmospheric conditions and seasonal and interannual variations. J. Clim. 29 (12), 4509–4523.

Klinck, J.M., 1996. Circulation near submarine canyons: A modeling study. J. Geophys. Res. Oceans 101 (C1), 1211–1223.

Kulikov, E., Carmack, E., Macdonald, R., 1998. Flow variability at the continental shelf break of the Mackenzie Shelf in the Beaufort Sea. J. Geophys. Res. Oceans 103 (C6), 12725–12741.

Li, M., Pickart, R.S., Spall, M.A., Weingartner, T.J., Lin, P., Moore, G., Qi, Y., 2019. Circulation of the Chukchi Sea shelfbreak and slope from moored timeseries. Oceanogr. Prog. https://doi.org/10.1016/j.pocean.2019.01.002.

Lin, P., Pickart, R.S., McRaven, L.T., Arrigo, K.R., Bahr, F., Lowry, K.E., Stockwell, D.A., Mordy, C.W., 2019a. Water mass evolution and circulation of the northeastern Chukchi Sea in summer: Implications for nutrient distributions. J. Geophys. Res. Oceans. 124, 4416–4432. https://doi.org/10.1029/2019JC015185.

Lin, P., Pickart, R.S., Moore, G., Spall, M.A., Hu, J., 2019b. Characteristics and dynamics of wind-driven upwelling in the Alaskan Beaufort Sea based on six years of mooring data. Deep Sea Res. II. https://doi.org/10.1016/j.dsr2.2018.01.002.

Lin, P., Pickart, R.S., Stafford, K.M., Moore, G., Torres, D.J., Bahr, F., Hu, J., 2016. Seasonal variation of the Beaufort shelfbreak jet and its relationship to Arctic cetacean occurrence. J. Geophys. Res. Oceans 121 (12), 8434–8454.

Lukovich, J., Barber, D., 2006. Atmospheric controls on sea ice motion in the southern Beaufort Sea. J. Geophys. Res.: Atmos. 111 (D18).

Macdonald, R., Wong, C., Erickson, P., 1987. The distribution of nutrients in the

southeastern Beaufort Sea: Implications for water circulation and primary production. J. Geophys. Res. Oceans 92 (C3), 2939–2952.
Martin, T., Steele, M., Zhang, J., 2014. Seasonality and long-term trend of Arctic Ocean surface stress in a model. J. Geophys. Res. Oceans 119 (3), 1723–1738.
McPhee, M.G., 2002. Turbulent stress at the ice/ocean interface and bottom surface hydraulic roughness during the SHEBA drift. J. Geophys. Res. Oceans 107 (C10) SHE 11–11-SHE 11–15.
Nikolopoulos, A., Pickart, R.S., Fratantoni, P.S., Shimada, K., Torres, D.J., Jones, E.P., 2009. The western Arctic boundary current at 152°W: Structure, variability, and transport. Deep Sea Res. II 56 (17), 1164–1181. https://doi.org/10.1016/j.dsr2.2008.10.014.
Pawlowicz, R., Beardsley, B., Lentz, S., 2002. Classical tidal harmonic analysis including error estimates in MATLAB using T_TIDE. Comput. Geosci. 28 (8), 929–937.
Pickart, R.S., 2004. Shelfbreak circulation in the Alaskan Beaufort Sea: Mean structure and variability. J. Geophys. Res. 109 (C4). https://doi.org/10.1029/2003jc001912.
Pickart, R.S., Moore, G., Mao, C., Bahr, F., Nobre, C., Weingartner, T.J., 2016. Circulation of winter water on the Chukchi shelf in early summer. Deep Sea Res. II 130, 56–75.
Pickart, R.S., Moore, G.W.K., Torres, D.J., Fratantoni, P.S., Goldsmith, R.A., Yang, J., 2009. Upwelling on the continental slope of the Alaskan Beaufort Sea: Storms, ice, and oceanographic response. J. Geophys. Res. 114. https://doi.org/10.1029/2008jc005009.
Pickart, R.S., Spall, M.A., Mathis, J.T., 2013. Dynamics of upwelling in the Alaskan Beaufort Sea and associated shelf–basin fluxes. Deep Sea Res. I 76, 35–51. https://doi.org/10.1016/j.dsr.2013.01.007.
Pickart, R.S., Spall, M.A., Moore, G.W.K., Weingartner, T.J., Woodgate, R.A., Aagaard, K., Shimada, K., 2011. Upwelling in the Alaskan Beaufort Sea: Atmospheric forcing and local versus non-local response. Prog. Oceanogr. 88, 78–100. https://doi.org/10.1016/j.pocean.2010.11.005.
Pisareva, M.N., Pickart, R.S., Spall, M., Nobre, C., Torres, D., Moore, G., Whitledge, T.E., 2015. Flow of Pacific water in the western Chukchi Sea: Results from the 2009 RUSALCA expedition. Deep Sea Res. I 105, 53–73.
Pite, H., Topham, D., Van Hardenberg, B., 1995. Laboratory measurements of the drag force on a family of two-dimensional ice keel models in a two-layer flow. J. Phys. Oceanogr. 25 (12), 3008–3031.
Rudels, B., Jones, E.P., Schauer, U., Eriksson, P., 2004. Atlantic sources of the Arctic Ocean surface and halocline waters. Polar Res. 23 (2), 181–208.
Schulze, L.M., Pickart, R.S., 2012. Seasonal variation of upwelling in the Alaskan Beaufort Sea: Impact of sea ice cover. J. Geophys. Res. Oceans 117 (C06022), n/a-n/a. https://doi.org/10.1029/2012jc007985.
Spall, M.A., Pickart, R.S., Li, M., Itoh, M., Lin, P., Kikuchi, T., Qi, Y., 2018. Transport of Pacific water into the Canada Basin and the formation of the Chukchi slope current. J. Geophys. Res. Oceans 123 (10), 7453–7471.
Spreen, G., Kaleschke, L., Heygster, G., 2008. Sea ice remote sensing using AMSR-E 89-GHz channels. J. Geophys. Res. Oceans 113 (C2).
Steele, M., Morison, J., Ermold, W., Rigor, I., Ortmeyer, M., Shimada, K., 2004. Circulation of summer Pacific halocline water in the Arctic Ocean. J. Geophys. Res. Oceans 109 (C2).
von Appen, W.-J., Pickart, R.S., 2012. Two configurations of the western Arctic shelfbreak current in summer. J. Phys. Oceanogr. 42 (3), 329–351.
Weingartner, T., Aagaard, K., Woodgate, R., Danielson, S., Sasaki, Y., Cavalieri, D., 2005. Circulation on the north central Chukchi Sea shelf. Deep Sea Res. II 52 (24), 3150–3174.
Weingartner, T.J., Danielson, S.L., Potter, R.A., Trefry, J.H., Mahoney, A., Savoie, M., Irvine, C., Sousa, L., 2017. Circulation and water properties in the landfast ice zone of the Alaskan Beaufort Sea. Cont. Shelf Res. 148, 185–198.
Williams, W.J., Carmack, E.C., 2008. Combined effect of wind-forcing and isobath divergence on upwelling at Cape Bathurst, Beaufort Sea. J. Mar. Res. 66 (5), 645–663.
Williams, W.J., Carmack, E.C., Shimada, K., Melling, H., Aagaard, K., Macdonald, R.W., Grant Ingram, R., 2006. Joint effects of wind and ice motion in forcing upwelling in Mackenzie Trough, Beaufort Sea. Cont. Shelf Res. 26 (19), 2352–2366. https://doi.org/10.1016/j.csr.2006.06.012.
Woodgate, R.A., 2018. Increases in the Pacific inflow to the Arctic from 1990 to 2015, and insights into seasonal trends and driving mechanisms from year-round Bering Strait mooring data. Prog. Oceanogr. 160, 124–154.
Woodgate, R.A., Aagaard, K., Weingartner, T.J., 2005. Monthly temperature, salinity, and transport variability of the Bering Strait through flow. Geophys. Res. Lett. 32 (L04601). https://doi.org/10.1029/2004gl021880.
Yang, J., 2006. The seasonal variability of the Arctic Ocean Ekman transport and its role in the mixed layer heat and salt fluxes. J. Clim. 19 (20), 5366–5387.